Rapid Communications

Defect transitions in nematic liquid-crystal capillary bridges

Perry W. Ellis, Shengnan Huang, Susannah Klaneček, Jayalakshmi Vallamkondu,[*] Edward Dannemiller, Mark Vernon,
Ya-wen Chang,[†] Paul M. Goldbart, and Alberto Fernandez-Nieves
School of Physics, Georgia Institute of Technology, Atlanta, Georgia 30332-0430, USA

(Received 31 July 2017; revised manuscript received 17 March 2018; published 13 April 2018)

We use experiment and computational modeling to understand the defect structure and director configuration in a nematic liquid crystal capillary bridge confined between two parallel plates. We find that tuning of the aspect ratio of the bridge drives a transition between a ring defect and a point defect. This transition exhibits hysteresis, due to the metastability of the point-defect structure. In addition, we see that the shape of the capillary-bridge surface determines whether the defect is hyperbolic or radial, with waistlike bridges containing hyperbolic defects and barrel-like bridges containing radial defects.

DOI: 10.1103/PhysRevE.97.040701

Uniaxial nematic liquid crystals (NLCs) are an ordered phase characterized by apolar orientational order where, on average, the individual mesogens align along a preferred axis, the director $\mathbf{n}$. As in other types of ordered media, defects in NLCs often appear as regions where the characteristic local order becomes undefined and are fundamental to the physics of the system [1]. Line defects, for example, can be entangled to both study knot theory [2,3] and generate topological materials [4,5], and point defects have been recently shown to mediate cell growth [6,7]. In addition, the understanding and control of defects in liquid-crystalline materials continues to yield technological developments, such as controlled self-assembly of colloidal particles [8–10] and new display technologies based on blue phases [11]. In all of these examples, confinement plays a significant role, as it introduces constraints that force the presence of defects in the director field. Clearly, confining a NLC to within a spherical volume and enforcing homeotropic boundary conditions, such that $\mathbf{n}$ is everywhere perpendicular to the surface, will result in at least one singularity within the volume. Because smooth deformations of $\mathbf{n}$ cannot remove a singularity, the defect is topological and can be characterized by its "hedgehog charge," defined as $Q = \frac{1}{4\pi}\int_{\mathbb{S}^2} d\theta\, d\phi\, \mathbf{n}\cdot[\partial_\theta \mathbf{n}\times\partial_\phi \mathbf{n}]$, where the integral is taken over a spherical surface enclosing the defect, and θ and ϕ are, respectively, the polar and azimuthal angles on that surface [12]. Geometrically, Q relates the orientations of $\mathbf{n}$ taken on a surface that is equivalent, topologically, to a sphere enclosing the defect to the number of times the orientations of $\mathbf{n}$ cover the unit sphere [12]. Thus, we see that confining a NLC to a volume that is topologically spherical with homeotropic boundary conditions must yield a total "hedgehog charge" $|Q| = 1$. This condition is satisfied by $Q = -1$ hyperbolic ring defects or hyperbolic point defects, shown from the side in the schematics in Figs. 1(a) and 1(d) and from the top in Figs. 1(c) and 1(f), and also by $Q = +1$ radial ring defects or radial point defects, shown from the side in the schematics in Figs. 1(b) and 1(e) and from the top in Figs. 1(c) and 1(f) [13].

The myriad of possible defect configurations gives topologically confined systems a richness that has been well explored for the case of geometrically spherical boundaries, where the confinement can only be modified through changing the sphere radius [14,15]. However, the role of shape when confining NLCs in geometries with more than one characteristic length scale is not completely understood. Consider the case of a cylindrical geometry of aspect ratio $\Gamma = 2R/H$, where R is the radius of the cylinder and H is its height. With this notation, the classic case of a cylindrical capillary corresponds to $\Gamma \ll 1$. The $\Gamma \gg 1$ situation corresponds to confinement between narrowly separated plates. When $\Gamma \sim O(1)$, the equilibrium defect configuration undergoes a transition from a ring defect, found when $\Gamma \gg 1$, to a point defect, seen when $\Gamma \ll 1$. Prior experimental work investigating this ring-to-point transition used liquid-crystal capillary bridges made with the NLC pentylcyanobiphenyl (5CB) [16,17]. However, since in Refs. [16,17], the bridge were only observed from above, where the radial and hyperbolic defect structures look similar, as demonstrated schematically in Figs. 1(c) and 1(f),

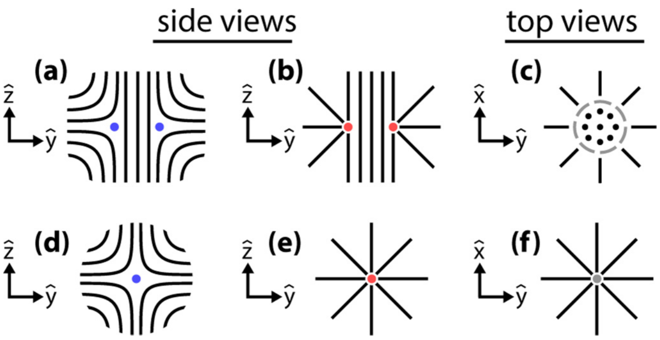

FIG. 1. (a,b,d,e) Cross sections of (a) hyperbolic and (b) radial rings, and of (d) hyperbolic and (f) radial point defects, viewed from the side. (c,f) Cross sections of (c) ring and (f) point defects, viewed from the top.

---

[*] Present address: Department of Physics, National Institute of Technology, Warangal, Telengana 506004, India.

[†] Present address: Department of Chemical Engineering, Texas Tech University, Lubbock, TX 79409-3121, USA.

they were unable to determine if the defects were radial or hyperbolic. Prior theoretical work used computational modeling to explore the defect configuration within a cylindrical bridge as a function of Γ and K_{11}/K_{33}, where K_{11} and K_{33} are the Frank elastic constants corresponding to splay and bend distortions, respectively [18,19]. For 5CB, which has $K_{11}/K_{33} = 0.74$, they predicted that the bridge should transition between a radial ring defect and a hyperbolic point defect. Since the capillary bridges in Refs. [16,17] were likely not cylindrical, the equilibrium defect configuration in nematic capillary bridges remains unknown.

In this Rapid Communication, we address this question and perform both experiments and computations pertaining to a confined NLC within a capillary bridge sandwiched between two parallel plates of adjustable separation and hence of varying Γ. By observing our experimental bridges from both the top and the side, and comparing our observations with results from our computations, we find that shape of the free surface controls whether the defect is radial or hyperbolic: waistlike bridges contain hyperbolic defects, and barrel-like bridges contain radial defects. In addition, we find good agreement between experiment and theory for the critical aspect ratio Γ_c at which the defect in the waist-shaped bridge undergoes a transition between a ring defect and a point defect. Finally, we see that this transition is hysteretic due to the metastability of the point defect. Our results clarify the role of shape and elasticity in dictating the defect structure in confined homeotropic nematics.

We first model a cylindrical nematic bridge using a modified version of the finite difference method laid out in Ref. [19]. Although the free energy in the algorithm presented there depends on the cut-off length of the defect core, the equilibrium defect configuration is independent of this length scale provided it is reasonably small. We modify the algorithm to treat the small region containing the defect separately from the remainder of the computation volume, such that the calculated free energy converges as the mesh size grows [20,24]. We find that a cylindrical bridge with $K_{11}/K_{33} = 0.74$ should undergo a defect transition between a radial ring and a hyperbolic point, as highlighted by the dashed line in the phase diagram in Fig. 2(a), consistent with prior computational modeling [19]. However, we predict ring-to-point defect transitions at aspect ratios that are significantly smaller than those in Ref. [19]. In addition, our phase diagram has no radial point structure, and the line separating the radial and hyperbolic rings occurs for $K_{11}/K_{33} < 1$ [see Fig. 2(a)]; these features are all in contrast to the diagram in Ref. [19], where there is a stable radial point and the transition between radial and hyperbolic rings always occurs at $K_{11}/K_{33} = 1$.

To address the problem experimentally, we confine 5CB (Hebei Mason Chemical Co.) between two parallel glass microscope slides (Thermo Scientific) to form a capillary bridge. Prior to use, the slides are dip coated with 0.1% w/w lecithin (granular; Acros) in hexane (98.5% purity; BDH) and left to dry to enforce homeotropic anchoring [25]. We set up the experiment by first placing both microscope slides stacked on top of each other on the microscope stage. We then epoxy the top plate to a rod affixed to a micromanipulator such that we can adjust the distance between the slides. Note that this simple protocol ensures that the two microscope slides are parallel to each other and to the microscope stage. After the epoxy hardens, we raise the top slide and use a glass capillary to place a ∼nl-volume drop of 5CB onto the bottom plate. We then bring the top plate down until it makes contact with the sessile droplet and forms a capillary bridge. The final experimental setup is depicted schematically from the side in Fig. 3(a).

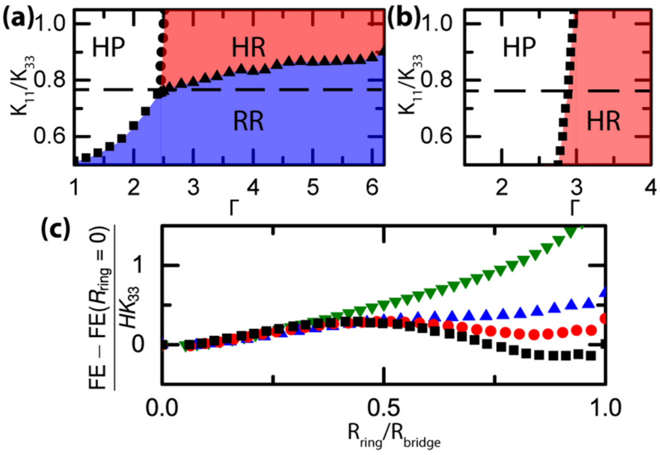

FIG. 2. (a,b) Phase diagram of the equilibrium defect structure in (a) a cylinder and (b) a waist-shaped bridge in terms of aspect ratio Γ and the ratio, K_{11}/K_{33}, of the splay and bend elastic constants. The dashed line indicates K_{11}/K_{33} for 5CB. HP: hyperbolic point; HR: hyperbolic ring; RR: radial ring. (c) Free energy of a director configuration in a waist-shaped bridge relative to the free energy in the presence of the point defect and normalized by HK_{33}, as a function of scaled ring radius $R_{\mathrm{ring}}/R_{\mathrm{bridge}}$. Squares: $\Gamma = 3.0$; circles: $\Gamma = 2.8$; up triangles: $\Gamma = 2.5$; down triangles: $\Gamma = 2.0$.

We can then view the bridge from the top and determine whether the defect is a ring or a point; examples of these situations are shown in the bright-field images in Figs. 3(b) and 3(d) and the corresponding crossed-polar images in Figs. 3(c) and 3(e). To calculate an effective aspect ratio Γ, we take R as the radius of the circular cross section of the bridge midway between the two confining plates, and H as the distance between the plates. We start at large Γ, where we observe a ring defect, and determine the radius of the ring, R_{ring}, as we decrease Γ by increasing H in discrete steps. At each H, we monitor the bridge over time to ensure that the defect state no longer changes and the system is in equilibrium. For each bridge, we also determine, as we decrease Γ, the effective aspect ratio for the defect transition, Γ_c. Using results for 21 different bridges, we find an average $\Gamma_c = 2.7 \pm 0.3$, as shown in the upper contour in Fig. 3(f), where we have plotted each observation of a stable ring defect with open circles and of a stable point defect with × symbols. The ring radius, scaled by the bridge height, varies linearly with Γ for $\Gamma > \Gamma_c$, as indicated by the squares in Fig. 3(g), where we have again plotted every measurement we have performed. At Γ_c, the ring becomes unstable, and collapses to a point defect, yielding the discontinuity in R_{ring} shown with a dashed line in Fig. 3(g), where the point defect is represented as having a vanishing R_{ring}.

To determine whether the defects are radial or hyperbolic we can look at the bridges from the side. We thus change our setup so that the microscope slides are held orthogonal to the

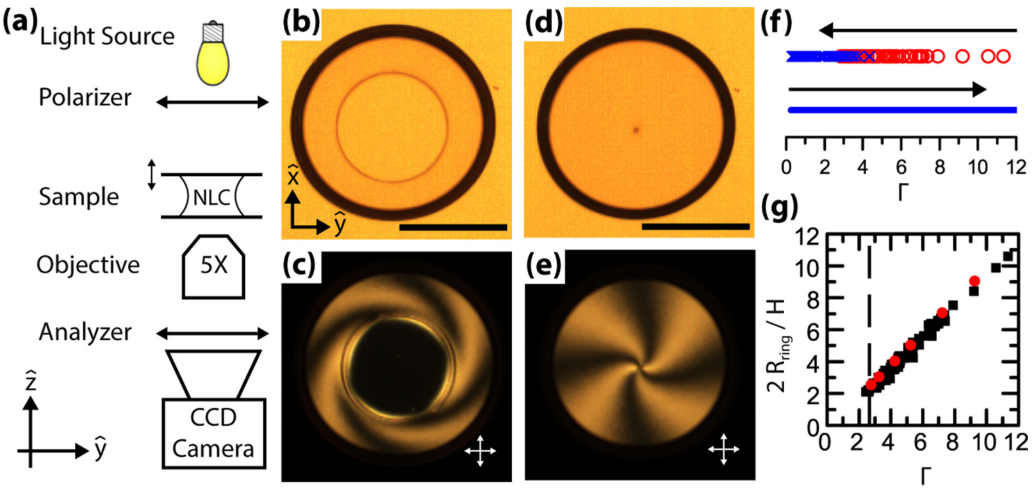

FIG. 3. (a) Schematic of the experimental setup with sample oriented for a top view. The distance between the plates can be increased and decreased, as indicated by the arrows near the top of the sample. (b–e) Example bright-field and crossed-polar images of a waist-shaped bridge with (b,c) ring and (d,e) point defects. (f) Experimental phase diagram for the defect state. Starting at a large Γ in the ring-defect state (open circles) and decreasing Γ leads to a transition to a point defect (× symbols) at a value of $\Gamma_c = 2.7 \pm 0.3$, which we obtain by averaging the result for all bridges. The error is the standard error of the mean. In contrast, when starting at small Γ in a point-defect state and increasing Γ, the point-defect state persists; this is represented with a line. (g) Twice the ring defect radius in a waist-shaped bridge scaled by height of the bridge, plotted as a function of the bridge aspect ratio. A vanishing ring radius corresponds to a point defect. The squares are experimental measurements. The circles correspond to computations in a waist structure using the elastic constants for 5CB. Scale bars in (b) and (d) are 250 μm.

microscope stage, as shown schematically in Supplemental Material Fig. S1(a) [20]. When viewed from the side, we first see that our bridges are waist shaped, as shown in the example bright-field image in Fig. 4(a), and are surfaces of constant mean curvature where the contact angle sets the shape [20]. We then rotate the crossed polarizer and analyzer to determine whether the defect is radial or hyperbolic. However, due to the curvature of the waist shape, we cannot clearly distinguish the rotation of the brushes. As an alternative to this approach, we introduce anisotropic fluorophores and use polarized epifluorescent microscopy (PFM) to see whether the defect is radial or hyperbolic, as shown schematically in Fig. S1(a) [20]. We add 0.01 wt % Nile red (Sigma Aldrich) to 5CB; at this concentration, Nile red does not affect the director configuration. Furthermore, the long axes of the fluorophores align along the director [26,27]. Because the emission dipole of Nile red lies along the long axis of the molecule, the fluorescent emission of the mixed Nile red and 5CB solution will be linearly polarized along the director [28]. We excite the sample with isotropic light from a short-arc lamp (X-Cite 120Q), and record the output color image as a function of analyzer angle Φ_A. We convert the color image to grayscale using a common weighted sum of the red (R), green (G), and blue (B) channels: 0.29889 R + 0.5870 G + 0.1140 B [29].

The emitted intensity from each point in the sample will be $\propto \cos^2(\Phi_A - \delta)$, where δ is the orientation of $\mathbf{n}$ in the plane of the output image [28]. As we use wide-field fluorescent microscopy, the intensity at each point in the output image reflects an averaging of the director along the light path. This technique is a simplified version of the polarized fluorescent confocal microscopy (PCFM) pioneered in Ref. [26]. Here, we sacrifice the three-dimensional spatial resolution of PCFM for the simplicity of PFM.

We validate our technique using a cylindrical capillary (World Precision Instruments) filled with Nile red–doped 5CB [20]. The capillary has an escaped-radial configuration with a point defect separating two regions that escape in the opposite direction [see Supplemental Material Fig. S1(b)] [20]. We find that we capture reasonably well the expected escaped-radial texture as well as the radial character of the defect between the two escaped domains [see Supplemental Material Fig. S1(c)], indicating that we can use PFM to determine if the defect in a bridge is hyperbolic or radial.

We then consider the example Nile red–doped NLC bridge seen under bright-field illumination in Fig. 4(a) and in PFM in Figs. 4(b)–4(d), where each image has already been converted to grayscale with the analyzer angle depicted schematically in the lower-right corner. For this example, we focus on the window of interrogation highlighted by the white square in Figs. 4(b)–4(d), and plot the mean grayscale intensity in this region as a function of analyzer angle, as shown in Fig. 4(e). We then fit this averaged output intensity, I, as a function of Φ_A in the window to the form

$$I = A + B\cos^2(\Phi_A - \delta'), \tag{1}$$

where A, B, and δ' are fitting parameters; A and B set the minimum value and range of I, respectively, and δ' reflects an average of the director orientation along the light path and over the window of interrogation. The side length of the window sets the spatial resolution of the technique; in all our experiments, we take a 10 px × 10 px window, which translates to a spatial resolution of 50 μm. From the fit, we find $\delta' = -45^\circ$. We do this for every window of interrogation in the whole image, and plot the director orientations on top of an epifluorescent image in Fig. 4(f). We find that the defect is clearly hyperbolic. Note that we are unable to distinguish the actual singularity due to

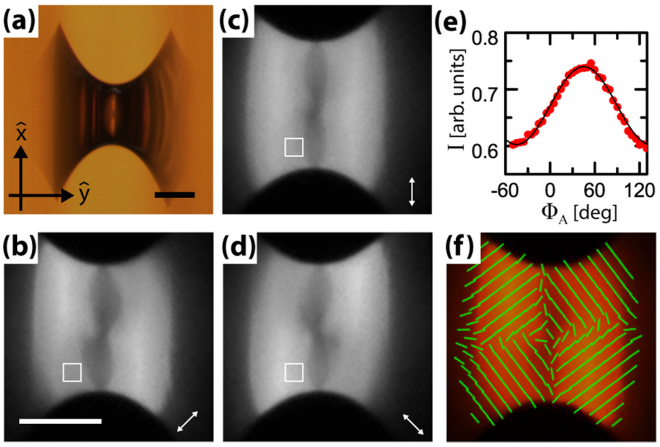

FIG. 4. (a) Bright-field image of a waist-shaped bridge. (b–d) Polarized epifluorescent images of the central region of the bridge in (a). The analyzer direction is indicated in the lower-right corner of the images. (e) Grayscale intensity I, as a function of analyzer angle ϕ_A, for the small square region highlighted in images (b–d). An intensity of 1 is mapped to white and 0 to black. The curve is a fit that allows us to obtain δ', and hence the approximate director in the region. (f) Director orientation plotted on top of an epifluorescent image with no analyzer in the emitted light path. Scale bars in (a) and (b) are 250 μm.

the wide-field nature of our technique and the spatial averaging; however, we clearly detect the presence of a hyperbolic defect in the bridge. We do this for bridges spanning $\Gamma \ll \Gamma_c$ to $\Gamma \gg \Gamma_c$, and find that the defect is always hyperbolic, implying that our bridges transition from a hyperbolic ring to a hyperbolic point as Γ decreases.

This transition appears to conflict with our computations, in which a radial ring is predicted to evolve into a hyperbolic point as Γ decreases for $K_{11}/K_{33} = 0.74$. However, the geometry in these computations is cylindrical. We therefore hypothesize that, due to the homeotropic boundary conditions, the shape of the boundary acts as a level surface for the director. Thus, the waistlike shape of the bounding surface of the bridges in our experiments will force any defect to be hyperbolic. To confirm this, we repeat our computations in a waistlike structure, and find that radial defects disappear for all values of K_{11}/K_{33} that we used, as shown in Fig. 2(b). Furthermore, we find that the ring defect radius predicted by our computations [circles, Fig. 3(g)] for a waistlike shape agrees well with our experimental data [squares, Fig. 3(g)]. In addition, we see that the hyperbolic ring to hyperbolic point transition happens at $\Gamma_c = 2.7$ for $K_{11}/K_{33} = 0.74$, in agreement with our experimental measurement for 5CB for decreasing Γ. However, we note that there is hysteresis in the experimental transition. When we start at $\Gamma < \Gamma_c$ in the point-defect state and increase Γ, the point defect never transitions to a ring, as seen in the lower contour in Fig. 3(f). Interestingly, if for $\Gamma > \Gamma_c$ we melt the nematic phase in a bridge containing a point defect, we always recover a ring defect state when we let the bridge cool back to the nematic phase. This suggests that the point defect is metastable for $\Gamma > \Gamma_c$. To test this possibility, we compute the energy landscape of a waist-shaped nematic bridge as a function of ring radius; we show the result for two bridges having $\Gamma > \Gamma_c$ and for two bridges having $\Gamma < \Gamma_c$ in Fig. 2(c), where we have taken $K_{11}/K_{33} = 0.74$. Recall that the point defect is represented by the free energy for a vanishing ring radius. We indeed see that the point defect is metastable for $\Gamma > \Gamma_c$, consistent with our interpretation of the experimental results. In addition, given a representative bridge height of $H = 100\ \mu$m and $K_{33} \approx 10^{-11}$ N, we note that the height of the barrier between the point and ring configurations, is always $O(10^4\, k_B T)$, implying that a point defect will not be observed to spontaneously transform into a ring defect, also consistent with our experimental observations. For $\Gamma < \Gamma_c$, this metastability disappears, and the point defect is the only stable defect state.

To further confirm that the shape of the bounding surface determines whether the defect is radial or hyperbolic, we examine barrel-shaped bridges. In this case, we expect that only radial defects should be present. In these experiments, we use Nile red–doped bridges with water as the outer medium. The water contains 8 mM sodium dodecyl sulfate (Sigma Aldrich) to enforce homeotropic anchoring. Viewed from the side, the bridge has a clear barrel shape, as shown by the bright-field image of an example bridge in Fig. S2(a) [20]. Just as all the waist-shaped bridges at all measured Γ contained hyperbolic defects, we find that all the barrel-shaped bridges at all measured Γ have radial defects. Viewed from the top, we only observe ring defect structures, as seen in the example barrel-shaped bridge in Supplemental Material Figs. S2(c) and S2(d) [20]. We have repeated our computations in a barrel-like structure, and find that the only stable state is a radial ring defect. This agrees with our experiments and further confirms that the shape of the bounding surface determines whether the enclosed defect structure is radial or hyperbolic.

In conclusion, the equilibrium defect structure in a nematic capillary bridge under homeotropic boundary conditions is found to depend on both the shape of the bounding surface as well as the aspect ratio of the bridge. The aspect ratio determines whether the defect is a ring defect or a point defect, and the boundary shape determines whether the defect is radial or hyperbolic, with waistlike shapes containing hyperbolic defects and barrel-like shapes containing radial defects. In addition, we find that in a waist structure the point defect can be metastable, causing the transition between a ring defect and a point defect to exhibit hysteresis. Starting at $\Gamma > \Gamma_c$ and decreasing Γ to below Γ_c brings about the collapse of the ring defect to a point defect, with the collapse occurring at a nonzero value of the ring radius. However, starting with a point defect at $\Gamma < \Gamma_c$ and increasing Γ never yields a transition from a point defect to a ring defect.

Although prior computations with thin films [30] or perforated sheets [31] have been used to attribute the radial or hyperbolic character of defects to confinement shape, our work provides experimental evidence of this phenomenon. We accomplish this by developing PFM, a simpler technique than its confocal counterpart that enables, despite refraction, the determination of the director field when viewing the bridge from the side. Thus, our work confirms that shape can be used to influence and control the equilibrium defect states in confined NLCs under homeotropic boundary conditions. Due to the ability of shape to bias the defect structure, the cylindrical bridge with $\Gamma \sim O(1)$ becomes an interestingly peculiar case, as the shape is neither a waist nor a barrel. In fact, our computations in a cylindrical bridge predict transitions from a radial ring to a hyperbolic point, as well as from a hyperbolic ring to a radial ring [see Fig. 2(a)], emphasizing the interesting scenarios that could arise for this shape; this would be technically difficult to investigate in our experiments, however, as one would need to enforce a θ of exactly $\pi/2$. Further interesting results in a cylinder include the sensitivity of the phase diagram in Fig. 2(a) to slight deviations from $\theta = \pi/2$ as well as the equilibrium shape of the bridge when nematic elasticity is comparable to or larger than the surface tension force [32]. In addition, the absence of a stable radial point defect in our phase diagrams regardless of the shape of the bridge is an intriguing feature that merits further work. Our work thus not only brings further understanding to the role of shape and elasticity in confined NLCs, but also highlights the relevance of future studies.

This work was supported by the National Science Foundation (DMR-1609841, DMR-1207026). P.W.E. and A.F.N. acknowledge funding from the FLAMEL program (NSF DGE-1258425). The work of P.M.G. was also performed in part at the Aspen Center for Physics (NSF PHY-1607611).

---

[1] N. W. Ashcroft and N. D. Mermin, *Solid State Physics* (Holt, Rinehart and Winston, New York, 2005).
[2] U. Tkalec, M. Ravnik, S. Čopar, S. Žumer, and I. Muševič, Science **333**, 62 (2011).
[3] S. Čopar, U. Tkalec, I. Muševič, and S. Žumer, Proc. Natl. Acad. Sci. USA **112**, 1675 (2015).
[4] T. A. Wood, J. S. Lintuvuori, A. B. Schofield, D. Marenduzzo, and W. C. K. Poon, Science **334**, 79 (2011).
[5] M. Ravnik, G. P. Alexander, J. M. Yeomans, and S. Žumer, Proc. Natl. Acad. Sci. USA **108**, 5188 (2011).
[6] A. Doostmohammadi, S. P. Thampi, and J. M. Yeomans, Phys. Rev. Lett. **117**, 048102 (2016).
[7] T. B. Saw, A. Doostmohammadi, V. Nier, L. Kocgozlu, S. Thampi, Y. Toyama, P. Marcq, C. T. Lim, J. M. Yeomans, and B. Ladoux, Nature (London) **544**, 212 (2017).
[8] D. R. Nelson, Nano Lett. **2**, 1125 (2002).
[9] P. Poulin, H. Stark, T. Lubensky, and D. Weitz, Science **275**, 1770 (1997).
[10] I. Muševič, M. Škarabot, U. Tkalec, M. Ravnik, and S. Žumer, Science **313**, 954 (2006).
[11] Y. Huang, H. Chen, G. Tan, H. Tobata, S.-i. Yamamoto, E. Okabe, Y.-F. Lan, C.-Y. Tsai, and S.-T. Wu, Opt. Mater. Express **7**, 641 (2017).
[12] G. P. Alexander, B. G.-g. Chen, E. A. Matsumoto, and R. D. Kamien, Rev. Mod. Phys. **84**, 497 (2012).
[13] We note that while the top view of the radial and hyperbolic defects appear the same in the schematics in Figs. 1(c) and 1(f), there are in reality subtle differences in the the molecular tilt that we have not depicted; see, e.g., M. V. Kurik and O. Lavrentovich, Physics-Uspekhi **31**, 3 (1988).
[14] P. S. Drzaic, *Liquid Crystal Dispersions* (World Scientific, Singapore, 1995), Vol. 1.
[15] T. Lopez-Leon and A. Fernandez-Nieves, Colloid Polym. Sci. **289**, 345 (2011).
[16] J. Gilli, S. Thiberge, A. Vierheilig, and F. Fried, Liq. Cryst. **23**, 619 (1997).
[17] S. Thiberge, C. Chevallard, J. Gilli, and A. Buka, Liq. Cryst. **26**, 1225 (1999).
[18] S.-H. Chen and B. Liang, Appl. Phys. Lett. **59**, 1173 (1991).
[19] B.-J. Liang and S.-H. Chen, J. Appl. Phys. **71**, 2189 (1992).
[20] See Supplemental Material at http://link.aps.org/supplemental/10.1103/PhysRevE.97.040701 for details on the numerical approach to cylindrical, waist-shaped and barrel-shaped bridges [21,22], and for additional experimental details on the shape of our bridges [23], the validation of polarized epifluorescent microscopy (PFM), and the configuration in barrel-shaped bridges.
[21] C. Williams, P. Pierański, and P. E. Cladis, Phys. Rev. Lett. **29**, 90 (1972).
[22] T. C. Lubensky, D. Pettey, N. Currier, and H. Stark, Phys. Rev. E **57**, 610 (1998).
[23] B. Lautrup, *Physics of Continuous Matter: Exotic and Everyday Phenomena in the Macroscopic World* (CRC Press, Boca Raton, 2011).
[24] W. H. Press, B. P. Flannery, S. A. Teukolsky, and W. T. Vetterling, *Numerical Recipes in C: The Art of Scientific Computing* (Cambridge University Press, Cambridge, 1996).
[25] K. Hiltrop and H. Stegemeyer, Mol. Cryst. Liq. Cryst. **49**, 61 (1978).
[26] I. I. Smalyukh, S. Shiyanovskii, and O. Lavrentovich, Chem. Phys. Lett. **336**, 88 (2001).
[27] I. I. Smalyukh, S. Chernyshuk, B. Lev, A. Nych, U. Ognysta, V. G. Nazarenko, and O. Lavrentovich, Phys. Rev. Lett. **93**, 117801 (2004).
[28] I. I. Smalyukh, B. I. Senyuk, M. Gu, and O. D. Lavrentovich, in *Congress on Optics and Optoelectronics* (International Society for Optics and Photonics, 2005), pp. 594707–594707-11.
[29] *Studio Encoding Parameters of Digital Television for Standard 4:3 and Wide-Screen 16:9* Aspect Ratios, Recommendation ITU-R BT.601-7, 2011.
[30] J. Ignés-Mullol, J. Baudry, L. Lejcek, and P. Oswald, Phys. Rev. E **59**, 568 (1999).
[31] L. Tran, M. O. Lavrentovich, D. A. Beller, N. Li, K. J. Stebe, and R. D. Kamien, Proc. Natl. Acad. Sci. USA **113**, 7106 (2016).
[32] L. Giomi, Phys. Rev. Lett. **109**, 136101 (2012).